Supplementary Information

Compositional Dependence of Hydrodeoxygenation Pathway Selectivity for $Ni_{2-x}Rh_xP$ Nanoparticle Catalysts

Nicole J. LiBretto[a†], Sean A. Tacey [a‡], Muhammad Zubair[b], Tuong V. Bui[a§], Kinga A. Unocic[c], Frederick G. Baddour[a], Michael B. Griffin[a], Joshua A. Schaidle[a], Carrie A. Farberow[a]*, Daniel A. Ruddy[a]*, Nicholas M. Bedford[b]*, and Susan E. Habas[a]*

[a] *National Renewable Energy Laboratory, Catalytic Carbon Transformation and Scale-up Center, Golden, CO, USA.*
[b] *University of New South Wales, School of Chemical Engineering, Sydney, NSW, AUS.*
[c] Oak Ridge National Laboratory, Center for Nanophase Materials Sciences, Oak Ridge, TN, USA.

*carrie.farberow@nrel.gov, *dan.ruddy@nrel.gov, *n.bedford@unsw.edu.au, *susan.habas@nrel.gov

Table of Contents

Methods

Materials. Synthetic manipulations to prepare transition metal phosphide (TMP) nanoparticles (NPs) were conducted under a N_2 atmosphere using standard Schlenk techniques or in an N_2-filled Vacuum Atmospheres glovebox, unless otherwise noted. ***Caution:*** *The metal phosphide precursors have the potential to evolve pyrophoric and/or toxic phosphorus species under reaction conditions. These reactions should only be performed by trained personnel under air-free conditions.* Oleylamine (OAm, 70%) and 1-octadecene (ODE) were purchased from Sigma-Alrich and dried prior to use by heating to 120 °C and 150 °C under vacuum, respectively, and were stored in an N_2-filled glovebox. Triphenylphosphine (PPh_3, 99%) was purchased from Sigma-Aldrich and used without further purification. The $Ni(CO)_2(PPh_3)_2$ and $RhCl(CO)(PPh_3)_2$ complexes were purchased from Strem Chemicals and used as received. The silica support (Sipernat-22) was provided by Evonik and calcined at 600 °C in flowing air prior to use. The Brunauer–Emmett–Teller (BET) surface area of the calcined silica support was measured as 190 $m^2\ g^{-1}$, and the aqueous incipient wetness point was determined to be 3.9 mL g^{-1}. Crushed quartz (150-250 and 300-425 micron, Powder Technologies Inc.) and silicon carbide (177-250 micron, McMaster Carr) were used as diluent materials during reactor testing. Guaiacol and *m*-cresol were obtained in high purity from Sigma-Aldrich, and acetone (HPLC grade) was obtained from Fischer Scientific. A certified gas blend of 5% argon/95% hydrogen was obtained from Air Liquide.

Characterization.

Scanning Transmission Electron Microscopy (STEM)

The TMP NPs were suspended in chloroform and drop-cast onto carbon-coated copper grids (Ted Pella part no. 01824). Image analysis and particle size distributions were obtained using ImageJ software.[1] Lattice spacings were measured from the fast-Fourier transforms (FFTs) of high-resolution STEM (HR-STEM) images. Size distributions were determined from a manual diameter measurement of >100 particles.

X-ray Diffraction (XRD) and simulated XRD patterns

Unsupported NPs were suspended in chloroform and drop-cast onto glass slides. The glass slide was loaded into the instrument at a fixed *z*-axis height. A NIST Si standard was used to calibrate shifts between diffraction patterns of different samples. Theoretical diffraction patterns were simulated at room temperature using crystal information files (cif) downloaded from the Inorganic Crystal Structure Database (ICSD) and imported to Materials Analysis Using Diffraction (MAUD) program,[2] which was used to identify the catalyst phase. A Rietveld refinement was performed in MAUD to fit the XRD patterns with varying amounts of Rh. By modifying the cif file of the parent binary Ni_2P structure to allow the identity of the Ni atoms to vary as either Ni or Rh, the location of the Rh atoms was determined. The lattice parameters (*a* and *c*) were also determined.

High Energy X-ray Diffraction (HE-XRD)/Atomic Pair Distribution Function (PDF)

In situ HE-XRD experiments were performed at the 6-ID-D beamline of the Advanced Photon Source (APS) at Argonne National Laboratory using an *in-situ* capillary heating cell.[3] The as-synthesized SiO_2-supported NPs were loaded into the capillary cell. HE-XRD patterns were

collected at room temperature, 350 °C in 5% H_2/Ar, and at 350 °C in guaiacol-saturated 5% H_2/Ar. A reciprocal space maximum, $Q_{max,}$ of ~28 $Å^{-1}$ was obtained using 100 keV X-rays. HE-XRD data were background corrected, transformed into reduced structure factors, and Fourier transformed into PDFs using PDFGETX3.[4]

Reverse Monte Carlo (RMC) simulations were performed on Ni_2P and $Ni_{1.6}Rh_{0.4}P$ using a spherical supercell of 65,953 atoms in a hexagonal Ni_2P lattice (~ 11.5 nm) as a starting structure, while Rh_2P was modeled starting with a 98,461 atom supercell (~12.5 nm) from the known cubic Rh_2P structure. The simulation sizes were selected based on nanpoarticle sizes observed from TEM. The initial configuration of $Ni_{1.6}Rh_{0.4}P$ was created by random distribution of Rh atoms in substitutional sites throughout the parent Ni_2P hexagonal supercell. RMC calculations were performed using the program fullrmc[5] by applying non-periodic boundary conditions with random move generator in any direction for all atom groups. The RMC models were refined by introducing constraints such as intramolecular pair distances from the experimental atomic PDFs. In $Ni_{1.6}Rh_{0.4}P$, a metal atom swapping function was implemented to prevent biasing of the final fitted structure by the original starting configuration. Further, the RMC simulated structures were analyzed by defining distance as a proxy for bonding environment. Average bond distances and coordination numbers were calculated from RMC-generated structures for all atoms that fall within the first coordination sphere (~3 Å).

Chemisorption. Catalyst samples (*ca.* 250 mg of SiO_2-supported material) were diluted with 750 mg of quartz chips and loaded into a quartz u-tube. The sample was dehydrated at 100 °C in flowing N_2 for 30 minutes, reduced in flowing UHP H_2 at 350 °C for 1 h (heating rate of 5 °C/min), and subsequently evacuated under vacuum for 8 h. H_2 chemisorption isotherms were measured at 150 °C over the pressure range of 200-800 torr. The site density (units of $\mu mol_{H*}/g_{cat}$, and converted to mol_{H*}/mol_M) was determined from the difference of the combined and weak isotherms extrapolated to zero pressure.

Catalyst Evaluation.

The conversion (X) was calculated as the difference between inlet and outlet molar flow rate of guaiacol or *m*-cresol, divided by the inlet molar flow rate of guaiacol or *m*-cresol as shown in Equation 1.

$$X = \frac{F_{liquidFeed-inlet} - F_{liquidFeed-outlet}}{F_{liquidFeed-inlet}} \quad (1)$$

Where $F_{liquidFeed-inlet}$ and $F_{liquidFeed-outlet}$ are the molar flow rates (mol/min) of guaiacol or *m*-cresol in the inlet and outlet streams, respectively.

The selectivity of product i (S_i) was defined as the ratio of outlet molar flow rate of product i (F_i) divided by the total outlet molar flow rate of all products as shown in Equation 2.

(2)

$$S_i = \frac{F_i}{\sum_{i=1}^{n} F_i}$$

The carbon selectivity of product i (SC_i) was calculated as the outlet carbon molar flow rate of product i (where C_i is the number of carbon atoms in component i and F_i is the outlet molar flow rate of component i) divided by the total outlet carbon molar flow rate of all products as shown in Equation 3.

$$SC_i = \frac{C_i \times F_i}{\sum_{i=1}^{n} C_i \times F_i} \tag{3}$$

Site-time yield (STY) was calculated according to Equation 4, where ρ_s is the H*-site density (mol_{H*}/g_{cat}), m_c is the catalyst mass (g_{cat}), and $\sum_{i=1}^{n} F_i$ is the sum of the outlet molar flow rates of each product (mol/min).

$$STY = \frac{\sum_{i=1}^{n} F_i}{\rho_s m_c} \tag{4}$$

Computational Methods

Ionic convergence was set to occur once the forces acting upon each atom fell below 0.02 eV/Å. The surface Brillouin zone was sampled using a 6 × 6 × 1 Monkhorst-Pack k-point meshes for the (1 × 1) surface models, while a 2 × 2 × 1 k-point mesh was utilized for the larger (3 × 3) $Ni_{2-x}Rh_xP(0001)$ and (4 × 4) $Rh_2P(100)$ surface unit cells. Adsorption was limited to one side of the slab models, with adsorbate-induced dipole corrections implemented in the z direction.[6,7]

The interaction between surface intermediates and the studied surfaces was described through the adsorption energy (E_B), in which

$$E_B = E_{tot} - E_{clean} - E_{gas}$$

where E_{tot}, E_{clean}, and E_{gas} are the energies of the adsorbate on the surface, the clean surface, and the adsorbate species in the gas-phase adsorbate, respectively. The electronic structures of Ni, Rh, and P atoms in the $Ni_{2-x}Rh_xP$ and Rh_2P model systems were evaluated using Bader charge analyses,[8–11] as well as *d*- and *sp*-band center calculations.[12,13]

Supplementary Experimental Data

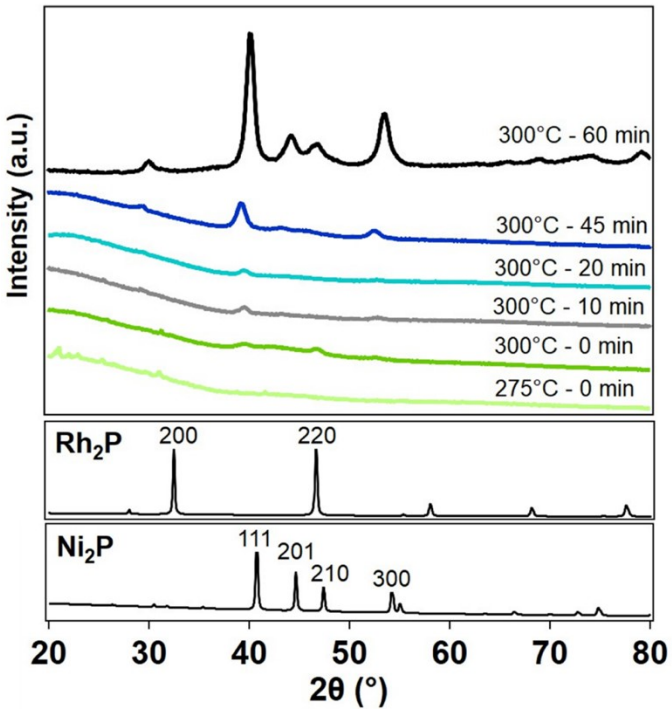

Figure S1. XRD patterns of aliquots taken during $Ni_{1.6}Rh_{0.4}P$ synthesis at increasing temperature and time, with reference patterns for Rh_2P and Ni_2P below.

Table S1. XRD reflections of unsupported $Ni_{2-x}Rh_xP$ NPs and vol% Rh_2P phase separation determined from Rietveld refinement analysis of experimental XRD patterns.

Targeted Composition	Major XRD reflections (°)	vol% cubic Rh_2P crystal structure
Ni_2P	40.8, 44.7, 47.4, 54.4	0
$Ni_{1.8}Rh_{0.2}P$	40.6, 44.6, 47.2, 54.4	0
$Ni_{1.6}Rh_{0.4}P$	40.3, 44.6, 47.0, 53.6	0
$Ni_{1.4}Rh_{0.6}P$	40.1, 44.5, 46.8,53.3	0
$Ni_{1.2}Rh_{0.8}P$	40.0, 44.5, 46.7, 53.2	3
$Ni_{1.0}Rh_{1.0}P$	32.7, 39.8, 47.3, 53.2, 59.1, 68.5	50
Rh_2P	32.2, 46.4, 55.3, 58.0, 68.1	100

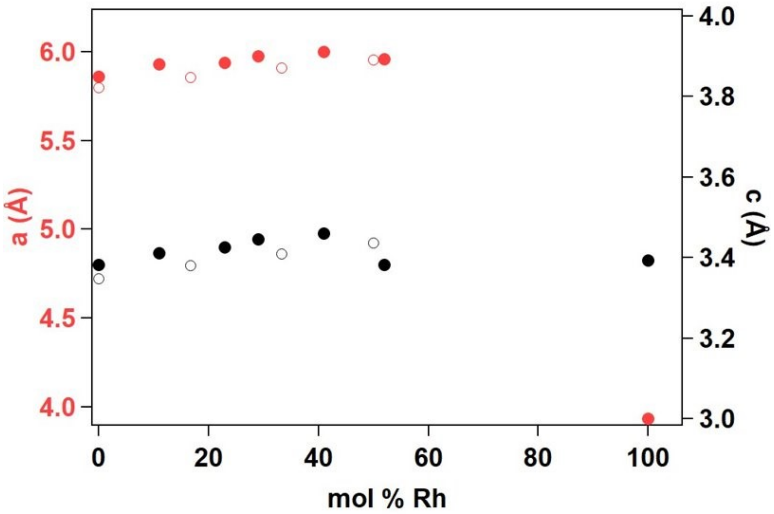

Figure S2. Lattice parameters *a* (red) and *c* (black) derived from experiment (solid) and DFT calculations (open) for the $Ni_{2-x}Rh_xP$ NPs as a function of measured Rh mol%.

Table S2. Measured (d_m) and reference (d_{ref}, 27162-ICSD) interplanar spacings, Bravais-Miller indices of the associated family of lattice planes (*hkil*), and measured and reference angles between designated reflections notated on the FFT of the high resolution HAADF-STEM image of $Ni_{1.6}Rh_{0.4}P$ NPs in Figure 2.

	d_m (Å)	d_{ref} (Å)	$hkil_{ref}$		$Angle_m$ (°)	$Angle_{ref}$ (°)
A	2.350	2.2143	$1\bar{2}11$	**AB**	43.54	44.40
B	2.342	2.2143	$\bar{1}121$	**BC**	68.13	67.80
C	3.156	2.9295	$\bar{2}110$	**CD**	68.34	67.80
D	2.350	2.2143	$\bar{1}2\bar{1}\bar{1}$	**DE**	43.53	44.40
E	2.342	2.2143	$11\bar{2}\bar{1}$	**EF**	68.13	67.80
F	3.156	2.9295	$2\bar{1}\bar{1}0$	**FA**	68.34	67.80

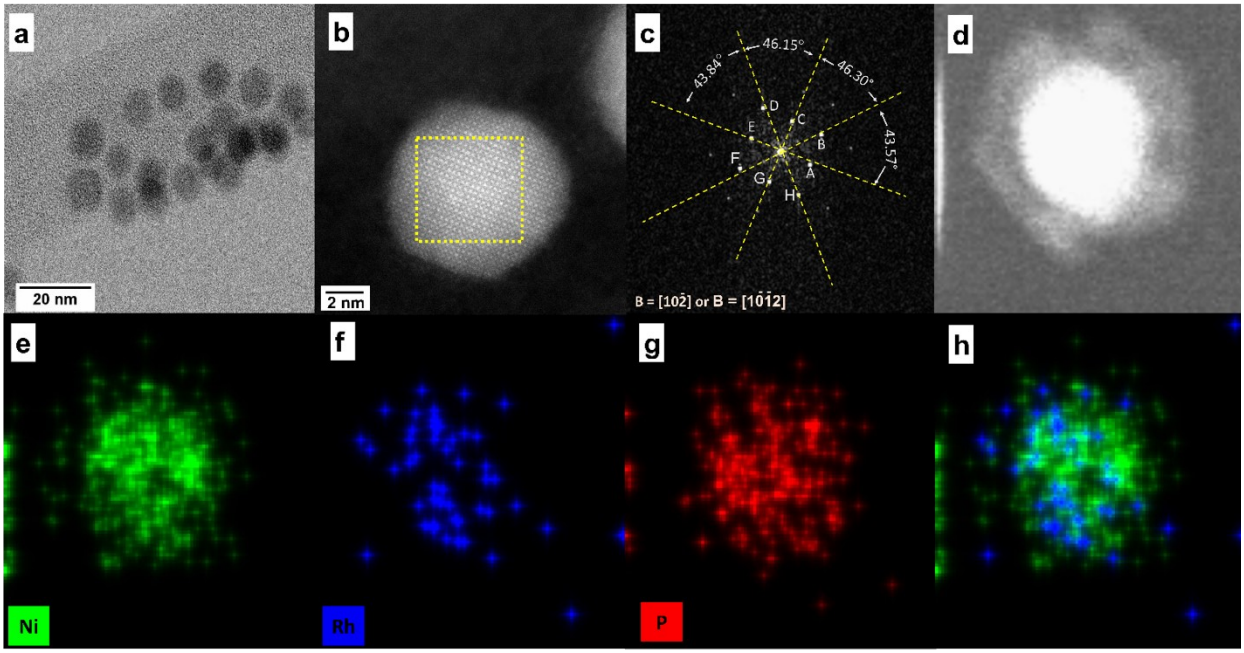

Figure S3. a) Bright field (BF)-STEM image of $Ni_{1.8}Rh_{0.2}P$ NPs, **b)** high resolution HAADF-STEM image with the **c)** FFT oriented along $[1\,0\,\bar{1}\,\bar{2}]$ direction. **d)** HAADF-STEM image for EDS analysis and associated EDS elemental maps for **e)** Ni **f)** Rh **g)** P, and **h)** Ni and Rh overlaid.

Table S3. Measured (d_m) and reference (d_{ref}, 27162-ICSD) interplanar spacings, Bravais-Miller indices of the associated family of lattice planes (*hkil*), and measured and reference angles between designated reflections notated on the FFT of the high resolution HAADF-STEM image of $Ni_{1.8}Rh_{0.2}P$ NPs in Figure S3.

	d_m (Å)	d_{ref} (Å)	$hkil_{ref}$		$Angle_m$ (°)	$Angle_{ref}$ (°)
A	2.825	2.8142	$1\,0\,\bar{3}\,1$	**AB**	43.31	43.85
B	2.060	2.0295	$0\,2\,\bar{2}\,1$	**BC**	46.73	46.15
C	2.988	2.9290	$\bar{1}\,2\,1\,0$	**CD**	46.30	46.15
D	2.051	2.0295	$\bar{2}\,2\,4\,\bar{1}$	**DE**	43.66	43.84
E	2.825	2.8142	$\bar{1}\,0\,3\,\bar{1}$	**EF**	43.69	43.85
F	2.060	2.0295	$0\,\bar{2}\,2\,\bar{1}$	**FG**	46.30	43.15
G	2.988	2.9290	$1\,\bar{2}\,\bar{1}\,0$	**GH**	46.50	43.15
H	2.051	2.0295	$2\,\bar{2}\,\bar{4}\,1$	**HA**	43.51	43.84

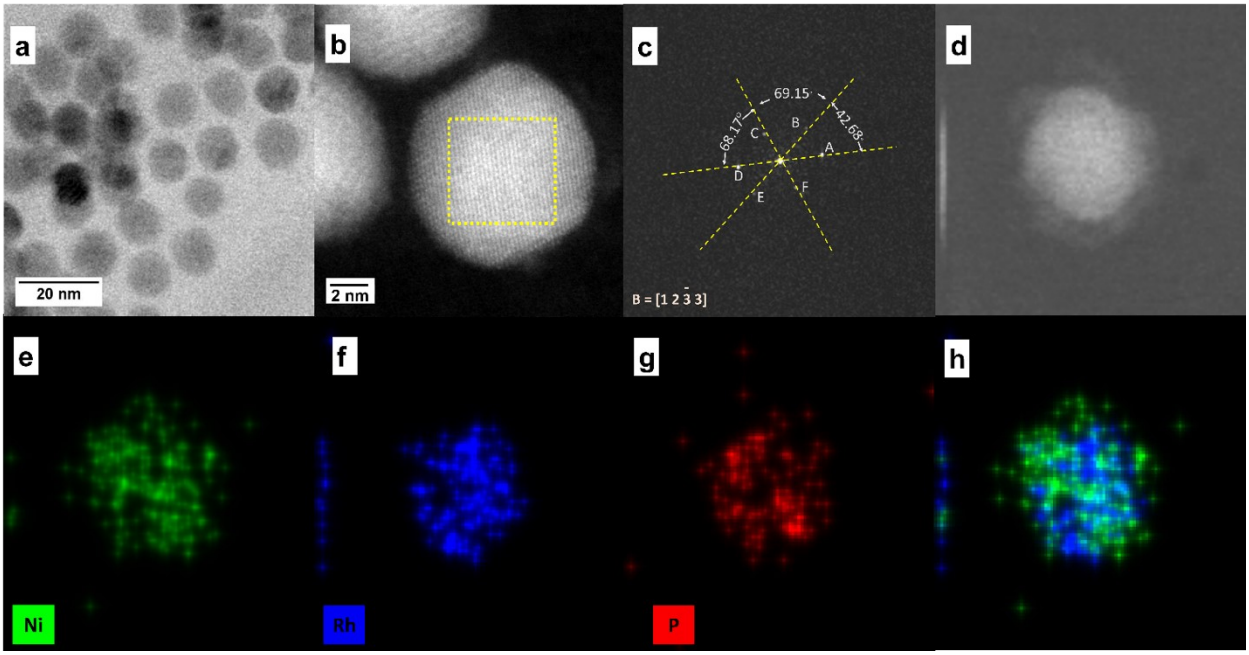

Figure S4. a) Bright field (BF)-STEM image of $Ni_{1.4}Rh_{0.6}P$ NPs, **b)** high resolution HAADF-STEM image with the **c)** FFT oriented along $[1\ 2\ \bar{3}\ 3]$ direction. **d)** HAADF-STEM image for EDS analysis and associated EDS elemental maps for **e)** Ni **f)** Rh **g)** P, and **h)** Ni and Rh overlaid.

Table S4. Measured (d_m) and reference (d_{ref}, 27162-ICSD) interplanar spacings, Bravais-Miller indices of the associated family of lattice planes (*hkil*), and measured and reference angles between designated reflections notated on the FFT of the high resolution HAADF-STEM image of $Ni_{1.4}Rh_{0.6}P$ NPs in Figure S4.

	d_m (Å)	D_{ref} (Å)	$hkil_{pdf}$		$Angle_m$ (°)	$Angle_{ref}$ (°)
A	2.281	2.214	$1\ \bar{2}\ 1\ 1$	**AB**	42.68	44.41
B	2.308	2.214	$\bar{1}\ \bar{1}\ 2\ 1$	**BC**	69.15	67.74
C	3.139	2.929	$\bar{2}\ 1\ 1\ 0$	**CD**	68.17	67.74
D	2.281	2.214	$\bar{1}\ 2\ \bar{1}\ 1$	**DE**	42.68	44.41
E	2.308	2.214	$1\ 1\ \bar{2}\ 1$	**EF**	69.15	67.74
F	3.139	2.929	$2\ \bar{1}\ \bar{1}\ 0$	**FA**	68.17	67.74

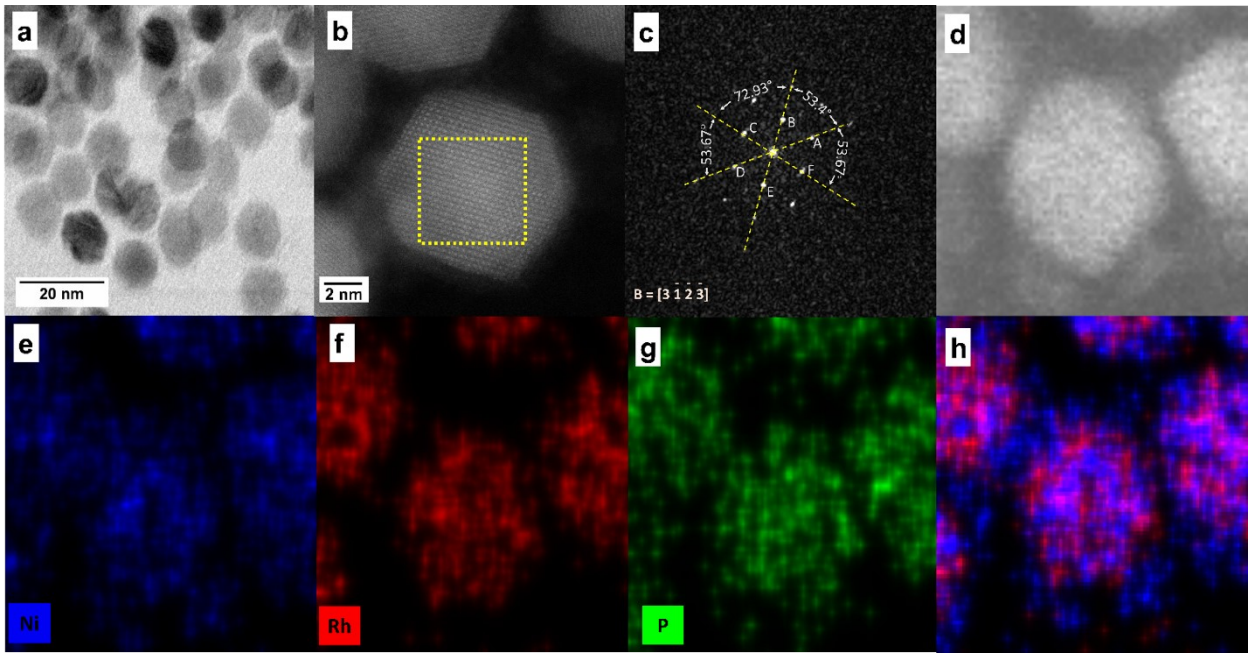

Figure S5. a) Bright field (BF)-STEM image of $Ni_{1.2}Rh_{0.8}P$ NPs, **b)** high resolution HAADF-STEM image with the **c)** FFT oriented along $[3\,\bar{1}\,2\,\bar{3}]$ direction. **d)** HAADF-STEM image for EDS analysis and associated EDS elemental maps for **e)** Ni **f)** Rh **g)** P, and **h)** Ni and Rh overlaid.

Table S5. Measured (d_m) and reference (d_{ref}, 27162-ICSD) interplanar spacings, Bravais-Miller indices of the associated family of lattice planes (*hkil*), and measured and reference angles between designated reflections notated on the FFT of the high resolution HAADF-STEM image of $Ni_{1.2}Rh_{0.8}P$ NPs in Figure S5.

	d_m (Å)	d_{ref} (Å)	$hkil_{ref}$		$Angle_m$ (°)	$Angle_{ref}$ (°)
A	2.509	2.219	$\bar{1}\,5\,4\,0$	**AB**	53.40	53.02
B	3.024	2.370	$4\,2\,\bar{6}\,0$	**BC**	72.93	73.49
C	2.978	2.693	$5\,\bar{3}\,\bar{2}\,1$	**CD**	53.67	53.47
D	2.509	2.219	$1\,\bar{5}\,4\,0$	**DE**	53.40	53.02
E	3.024	2.370	$\bar{4}\,\bar{2}\,6\,1$	**EF**	72.93	73.49
F	2.978	2.693	$\bar{5}\,3\,2\,1$	**FA**	53.67	53.47

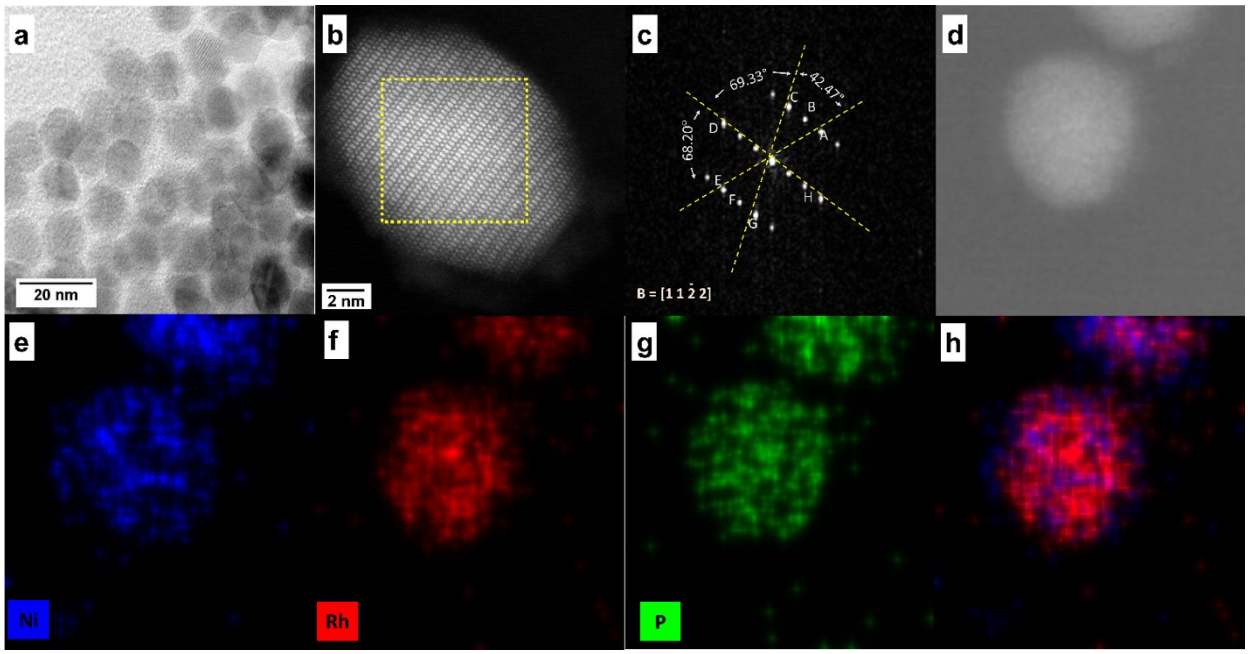

Figure S6. a) Bright field (BF)-STEM image of $Ni_{1.0}Rh_{1.0}P$ NPs, **b)** high resolution HAADF-STEM image with the **c)** FFT oriented along [1122] direction. **d)** HAADF-STEM image for EDS analysis and associated EDS elemental maps for **e)** Ni **f)** Rh **g)** P, and **h)** Ni and Rh overlaid.

Table S6. Measured (d_m) and reference (d_{ref}, 27162-ICSD) interplanar spacings, Bravais-Miller indices of the associated family of lattice planes (*hkil*), and measured and reference angles between designated reflections notated on the FFT of the high resolution HAADF-STEM image of $Ni_{1.0}Rh_{1.0}P$ NPs in Figure S6.

	d_m (Å)	d_{ref} (Å)	$hkil_{ref}$		$Angle_m$ (°)	$Angle_{ref}$ (°)
A	2.304	2.029	0 2 $\bar{2}$ $\bar{1}$	**AB**	21.12	23.57
B	2.481	2.214	1 1 $\bar{2}$ $\bar{1}$	**BC**	21.35	23.57
C	2.324	2.029	2 0 $\bar{2}$ $\bar{1}$	**CD**	69.33	66.42
D	6.364	5.074	1 $\bar{1}$ 0 0	**DE**	68.20	66.42
E	2.304	2.029	0 $\bar{2}$ 2 1	**EF**	21.12	23.57
F	2.481	2.214	$\bar{1}$ $\bar{1}$ 2 1	**FG**	21.35	23.57
G	2.324	2.029	$\bar{2}$ 0 2 1	**GH**	69.33	66.42
H	6.364	5.074	$\bar{1}$ 1 0 0	**HA**	68.20	66.42

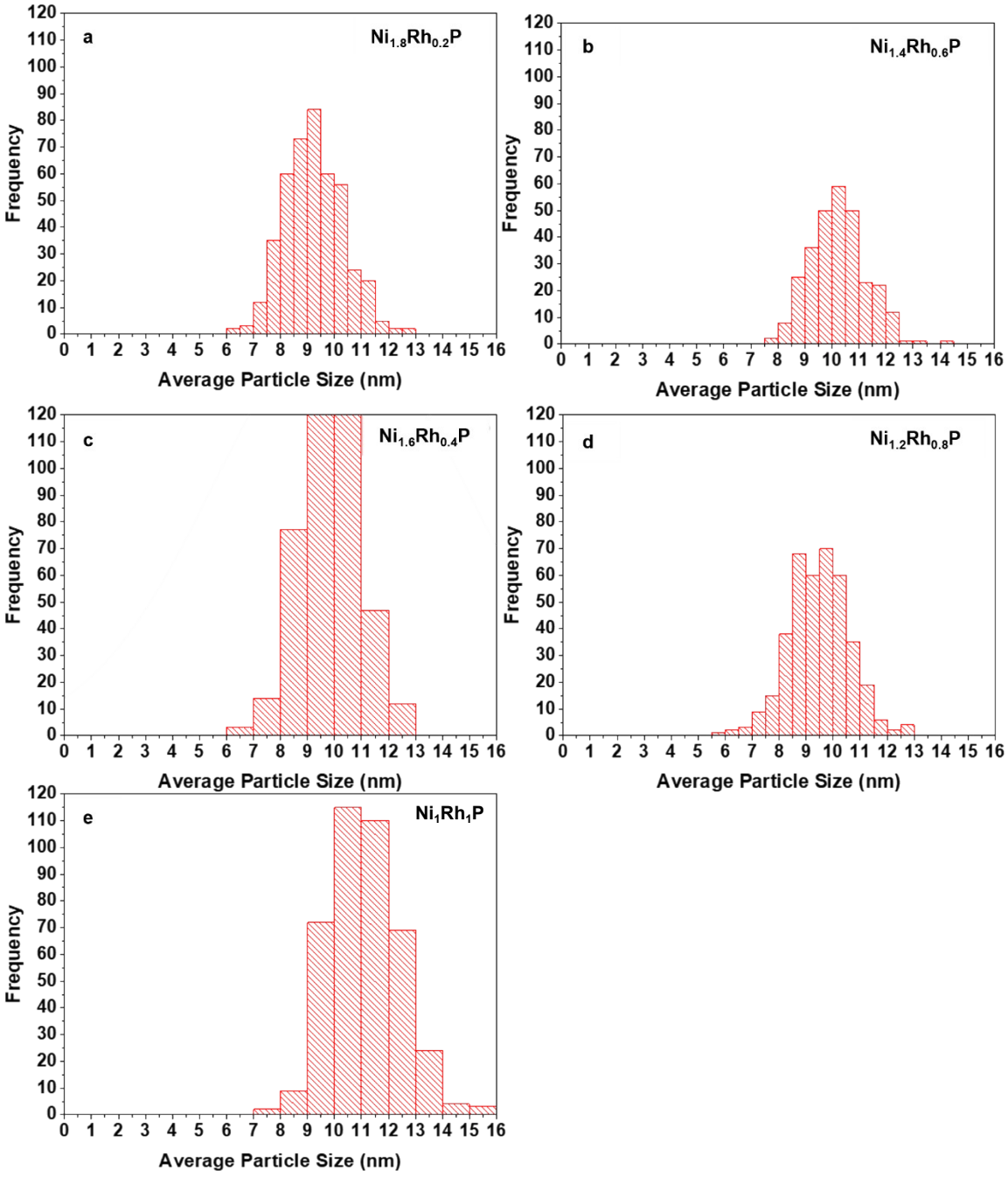

Figure S7. Particle size distributions measured from STEM images of **a)** $Ni_{1.8}Rh_{0.2}P$ **b)** $Ni_{1.6}Rh_{0.4}P$ **c)** $Ni_{1.4}Rh_{0.6}P$ **d)** $Ni_{1.2}Rh_{0.8}P$ and **e)** $Ni_{1.0}Rh_{1.0}P$ NPs.

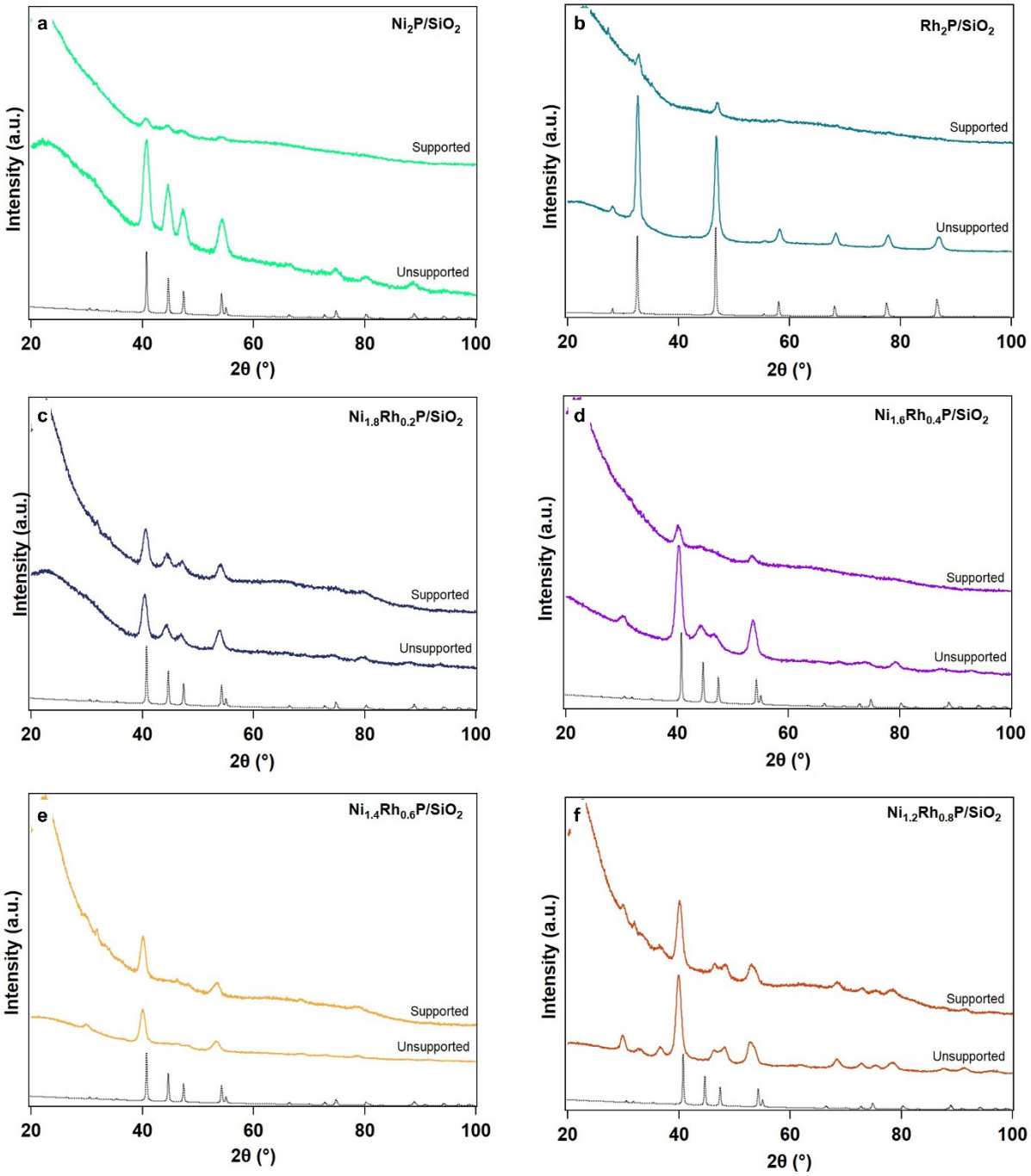

Figure S8. XRD patterns of unsupported and silica-supported **a)** Ni_2P, **b)** Rh_2P, **c)** $Ni_{1.8}Rh_{0.2}P$, **d)** $Ni_{1.6}Rh_{0.4}P$, **e)** $Ni_{1.4}Rh_{0.6}P$, and **f)** $Ni_{1.2}Rh_{0.8}P$ NPs with associated reference patterns. Each material contains *ca*. 5 wt% $Ni_{2-x}Rh_xP$.

Table S7. Summary of properties of SiO_2-supported TMP catalysts including particle size determined by XRD, and weight loadings and and molar ratios determined by inductively coupled plasma-optical emission spectroscopy.

Sample	XRD size (nm)	wt% Ni	wt% Rh	wt% P	wt% active phase	Rh/Ni Molar Ratio	M/P Molar Ratio
Ni_2P	9.8	3.47	-	1.15	4.4	-	1.59
$Ni_{1.8}Rh_{0.2}P$	8.8	3.15	0.67	1.18	4.7	0.12	1.59
$Ni_{1.6}Rh_{0.4}P$	9.1	2.34	1.25	0.90	4.2	0.31	1.78
$Ni_{1.4}Rh_{0.6}P$	9.0	2.33	1.67	0.99	4.6	0.41	1.76
$Ni_{1.2}Rh_{0.8}P$	9.6	1.84	2.26	0.90	4.6	0.70	1.83
Rh_2P	11.6	-	3.66	0.70	4.2	-	1.58

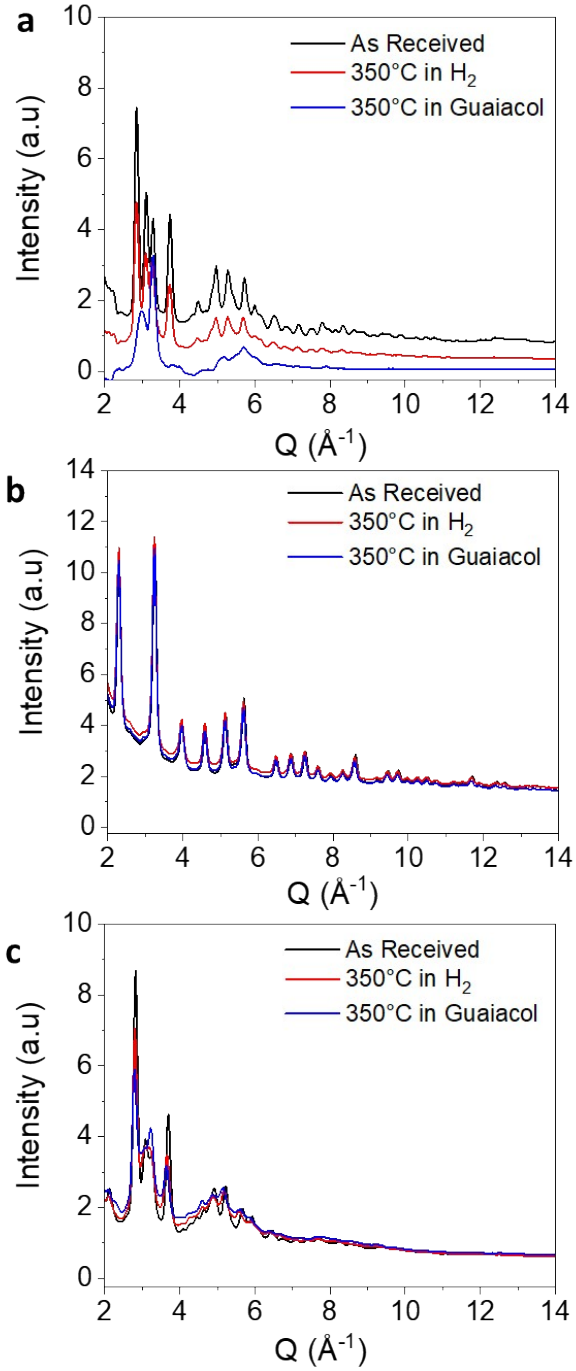

Figure S9. *In-situ* HE-XRD reciprocal space raw data at ambient temperature, 350 °C in H_2, and 350 °C in guaiacol and H_2 for **a)** Ni_2P/SiO_2, **b)** Rh_2P/SiO_2, and **c)** $Ni_{1.6}Rh_{0.4}P/SiO_2$.

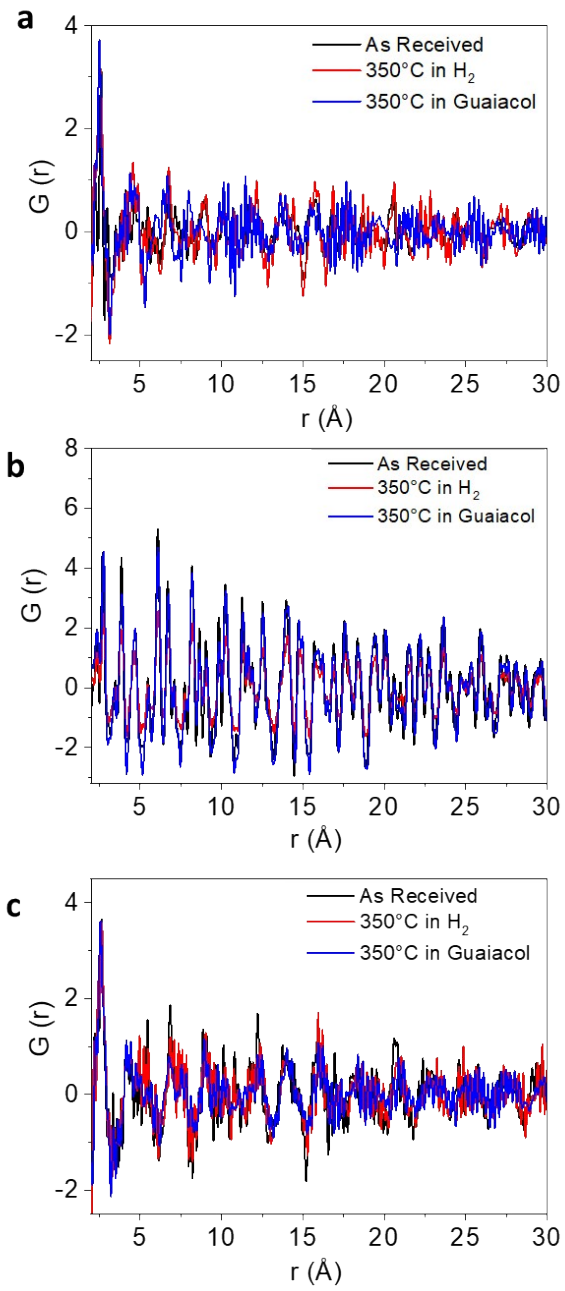

Figure S10. Long range PDFs at ambient temperature, 350 °C in H_2, and 350 °C in guaiacol and H_2 for **a)** Ni_2P/SiO_2 **b)** Rh_2P/SiO_2 and **c)** $Ni_{1.6}Rh_{0.4}P/SiO_2$.

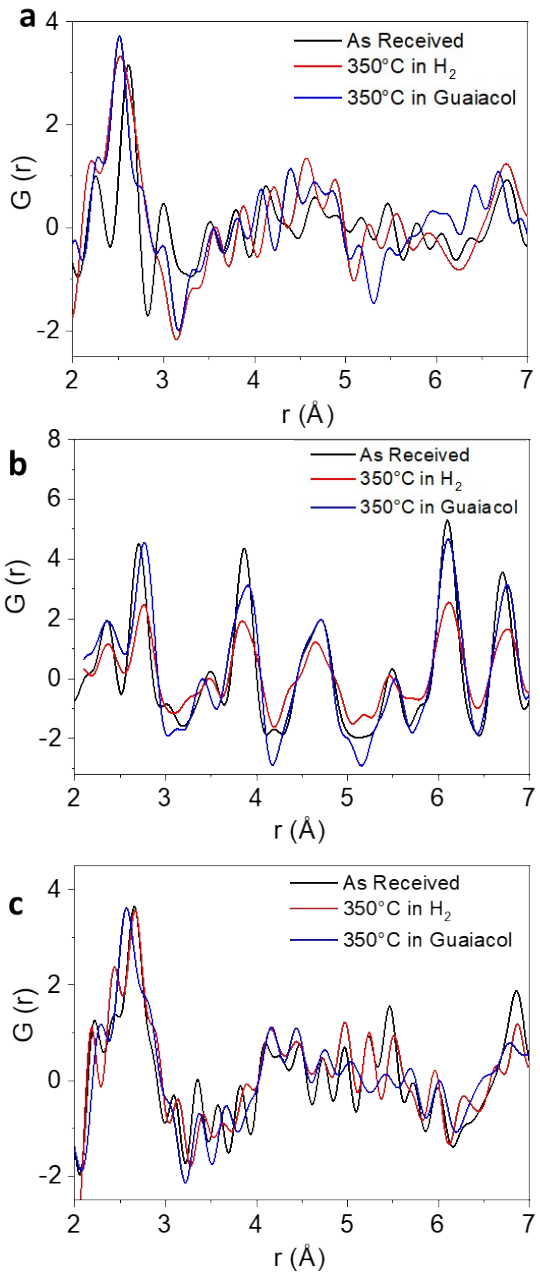

Figure S11. Short range PDFs at ambient temperature, 350 °C in H_2, and 350 °C in guaiacol and H_2 for **a)** Ni_2P/SiO_2 **b)** Rh_2P/SiO_2 and **c)** $Ni_{1.6}Rh_{0.4}P/SiO_2$.

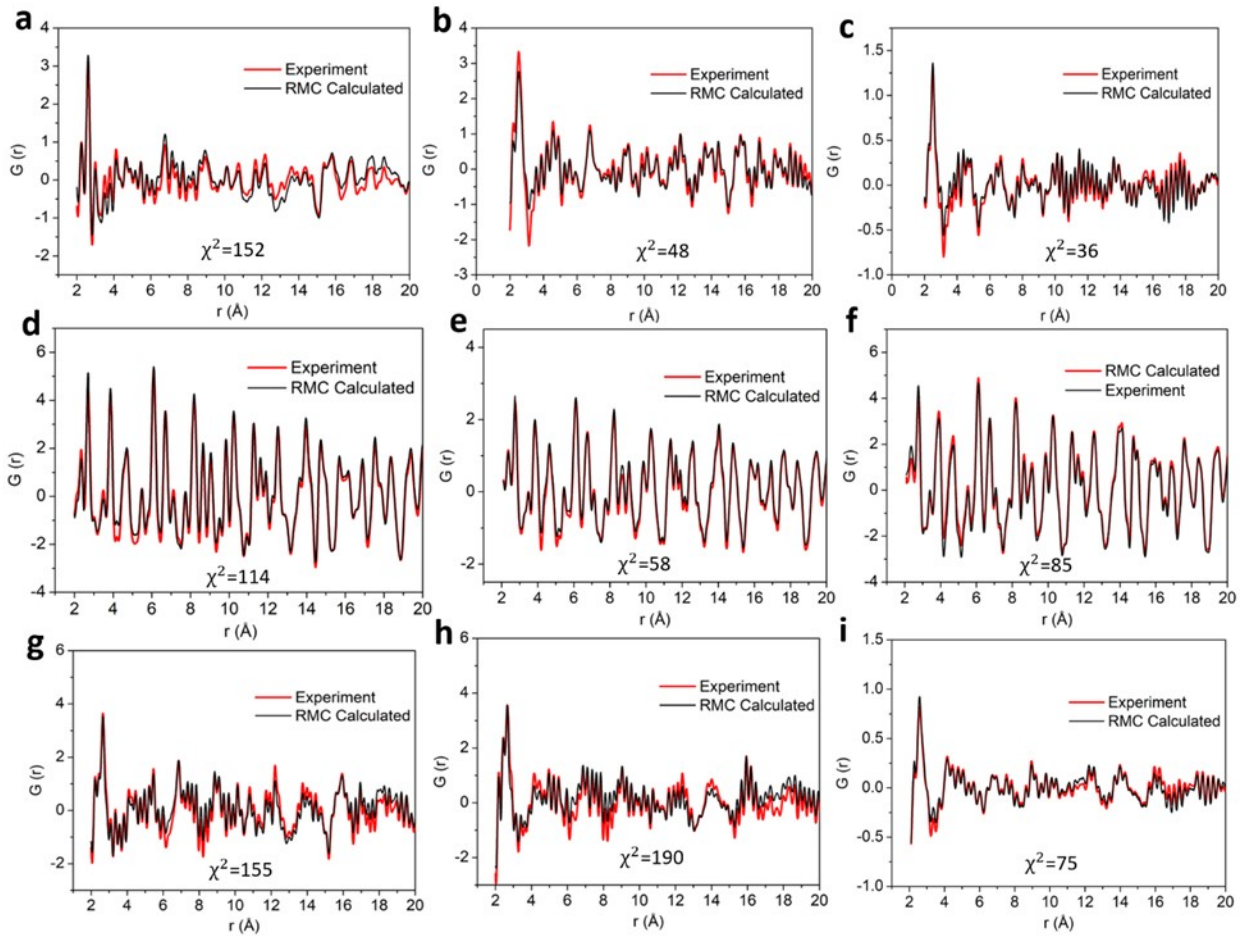

Figure S12. RMC fits for **a)** Ni_2P/SiO_2 at room temperature, **b)** Ni_2P/SiO_2 at 350 °C in H_2, **c)** Ni_2P/SiO_2 at 350 °C in guaiacol and H_2, **d)** Rh_2P/SiO_2 at ambient temperature, **e)** Rh_2P/SiO_2 at 350°C in H_2, **f)** Rh_2P/SiO_2 at 350 °C in guaiacol and H_2, **g)** $Ni_{1.6}Rh_{0.4}P/SiO_2$ at ambient temperature, h) $Ni_{1.6}Rh_{0.4}P/SiO_2$ at 350 °C in H_2, and **i)** $Ni_{1.6}Rh_{0.4}P/SiO_2$ at 350 °C in guaiacol and H_2.

Table S8. Summary of structural parameters including average coordination number, average bond length, and ratio of M-M to M-P coordination numbers at ambient temperature, 350 °C in H_2, and 350 °C in guaiacol and H_2 from RMC simulations, shown in Figures S13, S14, and S15, below.

Sample	Scattering Pair	Room Temperature			350 °C H_2			350 °C Guaiacol		
		CN	R(Å)	M-M/ M-P	CN	R(Å)	M-M/ M-P	CN	R(Å)	M-M/ M-P
Ni_2P/SiO_2	Ni-P	2.35	2.30	1.45	2.15	2.30	1.63	2.00	2.27	1.7
	Ni-Ni	3.40	2.63		3.45	2.60		3.4	2.56	
$Ni_{1.6}Rh_{0.4}P/SiO_2$	Ni-P	2.15	2.35	1.48	2.00	2.35	1.65	2.00	2.32	1.66
	Ni-Ni	3.07	2.65		3.35	2.65		3.40	2.61	
	Rh-P	2.30	2.42		2.12	2.45		2.12	2.40	
	Ni-Rh	0.38	2.69		0.39	2.69		0.35	2.67	
	Rh-Ni	1.45	2.69		1.47	2.69		1.33	2.67	
	Rh-Rh	2.08	2.69		2.00	2.69		2.1	2.68	
Rh_2P/SiO_2	Rh-P	2.70	2.40	1.30	2.13	2.41	1.40	2.05	2.40	1.51
	Rh-Rh	3.00	2.70		3.00	2.72		3.10	2.75	

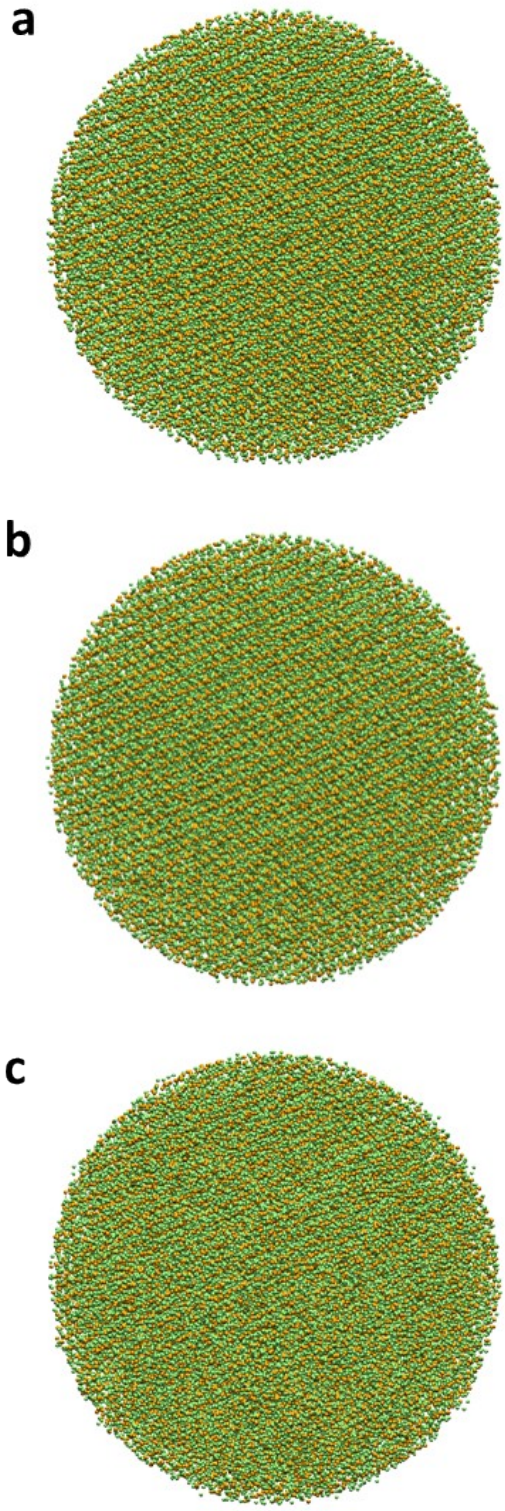

Figure S13. RMC models for Ni_2P/SiO_2 at **a)** ambient temperature, **b)** 350 °C in H_2, and **c)** 350 °C in guaiacol and H_2.

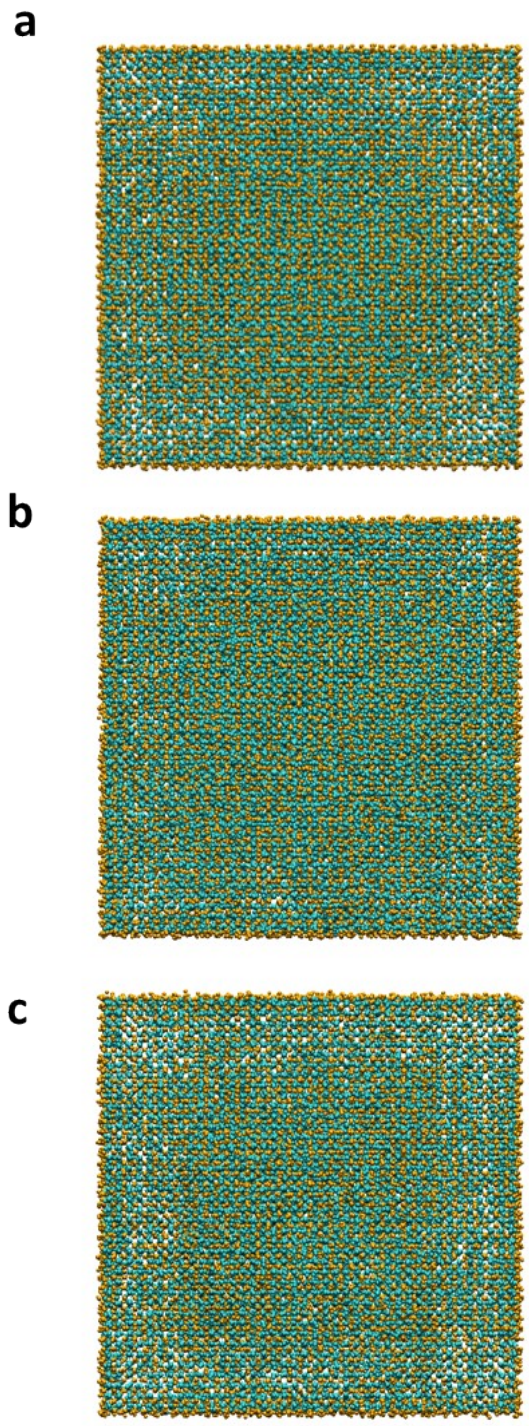

Figure S14. RMC models for Rh_2P/SiO_2 at **a)** ambient temperature, **b)** 350 °C in H_2, and **c)** 350 °C in guaiacol and H_2.

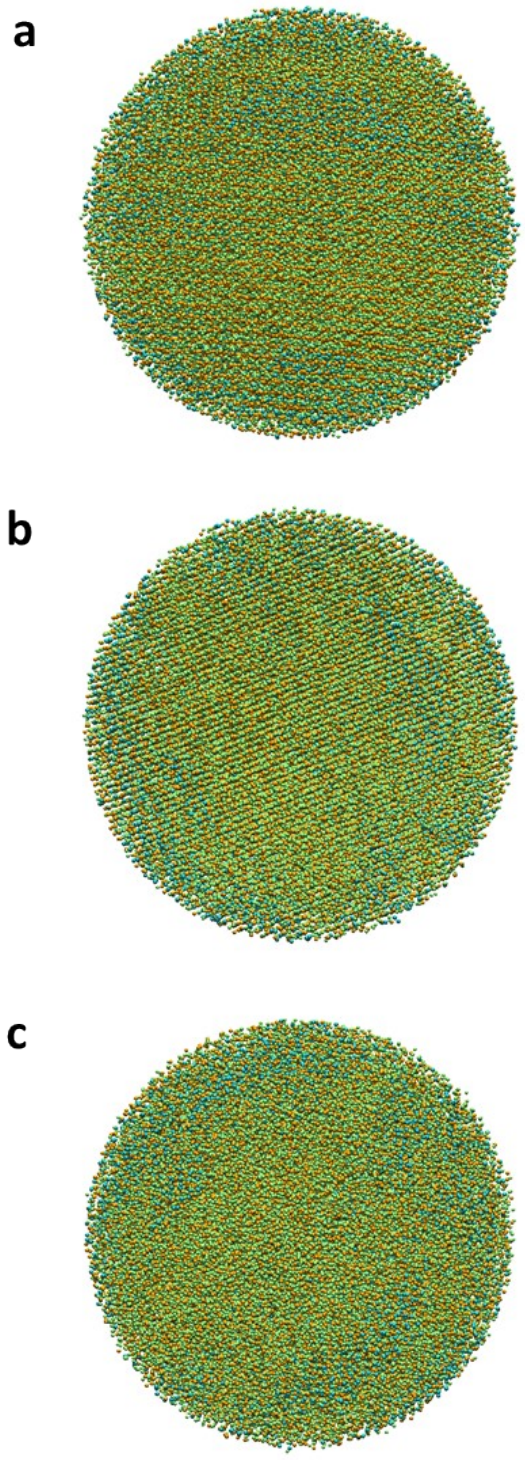

Figure S15. RMC models for $Ni_{1.6}Rh_{0.4}P/SiO_2$ at **a)** ambient temperature, **b)** 350 °C in H_2, and **c)** 350 °C in guaiacol and H_2.

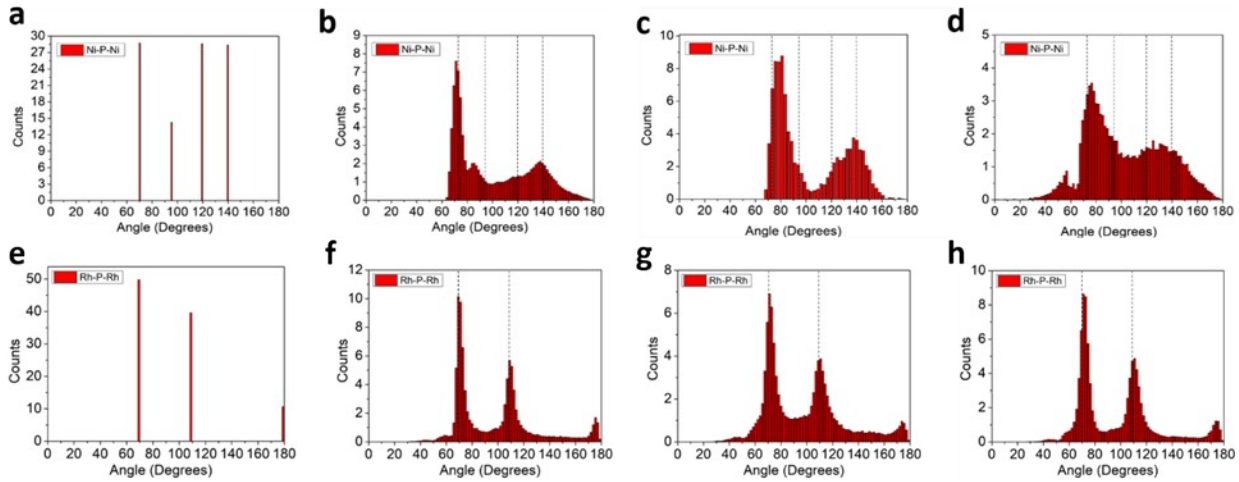

Figure S16. Bond angle distributions (Metal-P-Metal) for **a)** ideal Ni_2P hexagonal structure, **b)** Ni_2P at ambient temperature, **c)** Ni_2P at 350 °C in H_2, **d)** Ni_2P at 350 °C in guaiacol, **e)** ideal Rh_2P cubic structure, **f)** Rh_2P at ambient temperature, **g)** Rh_2P at 350 °C in H_2, and **h)** Rh_2P at 350 °C in guaiacol. Dashed vertical lines represent angles for ideal hexagonal Ni_2P or cubic Rh_2P crystal structures.

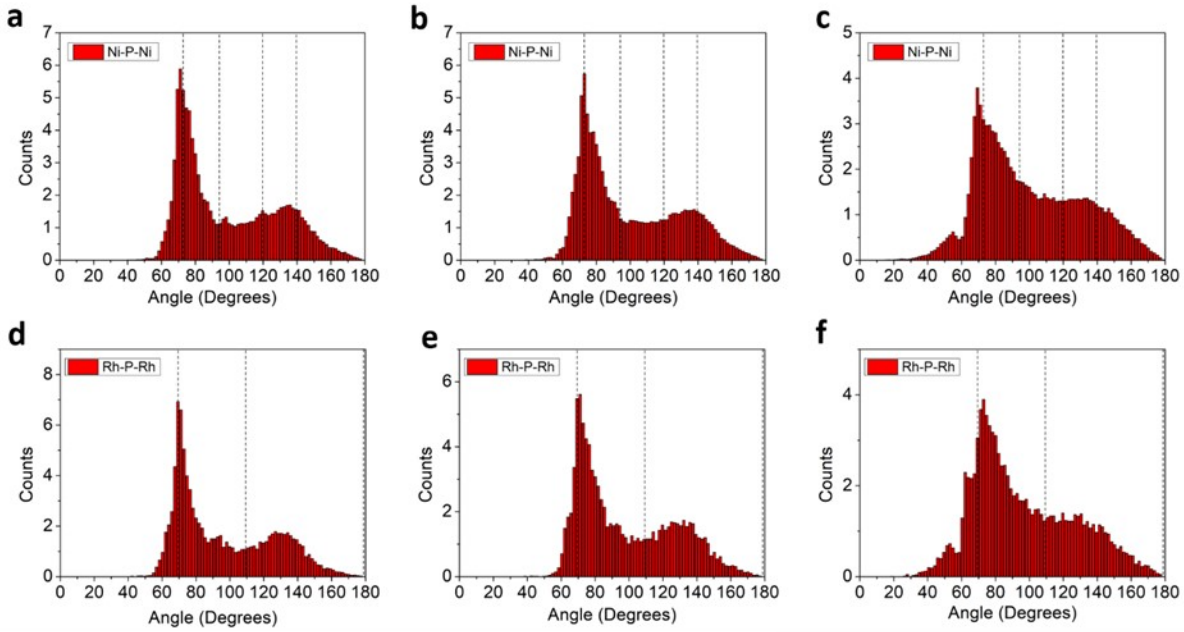

Figure S17. a,b,c) Ni-P-Ni angle distribution in $Ni_{1.6}Rh_{0.4}P$ at ambient temperature, 350 °C in H_2 and 350 °C in guaiacol respectively. **d,e,f)** Rh-P-Rh angle distribution in $Ni_{1.6}Rh_{0.4}P$ at ambient temperature, 350 °C in H_2 and 350 °C in guaiacol, respectively. Dashed vertical lines represent angles for ideal hexagonal Ni_2P or cubic Rh_2P crystal structures.

Table S9. Peak fitting analysis of bond angle distributions for Ni_2P and $Ni_{1.6}Rh_{0.4}P$ shown in Figure S16, where x_o indicates the peak position and deviation from ideal structure.

	FWHM (Ni-P-Ni)	x_o
Ni_2P/SiO_2		
Ambient Temperature	7.76 ± 0.69	74.64 ± 0.29
350 °C in H_2	13.22 ± 1.29	79.06 ± 0.53
350 °C in Guaiacol	23.08 ± 2.65	80.42 ± 1.06
$Ni_{1.6}Rh_{0.4}P/SiO_2$		
Ambient Temperature	18.46 ± 1.32	80.76 ± 0.53
350 °C in H_2	23.26 ± 1.70	83.01 ± 0.68
350 °C in Guaiacol	45.08 ± 2.81	88.91 ± 0.99

Table S10. Catalytic performance data from the guaiacol HDO reaction at 350 °C, 0.5 MPa, 12:1 H_2:guaiacol molar ratio, WHSV = 5 h^{-1}, presented as an average between 290 and 460 min time-on-stream for SiO_2-supported Ni_2P, $Ni_{1.6}Rh_{0.4}P$, and Rh_2P catalysts.

	Ni_2P	**$Ni_{1.6}Rh_{0.4}P$**	**Rh_2P**
Conversion (%)	14.0	17.7	13.7
STY (1/s)	13.7 x 10^{-2}	16.6 x 10^{-2}	6.4 x 10^{-2}
Total Carbon Product Selectivity (%)			
2-Methoxycyclohexanone	3.92	3.8	0.92
1,2-Dimethoxy Benzene	-	1.46	3.41
Catechol	-	7.24	2.94
Cyclohexanol	1.99	2.96	0.73
Cyclohexanone	7.91	7.30	2.51
Anisole	9.33	7.47	12.3
Phenol	41.9	47.6	64.2
Methanol	4.67	4.93	3.4
Benzene	1.39	0.84	0.67
Cyclohexane	11.0	5.77	2.82
Cyclohexene	5.82	2.22	0.81
1-Methoxy 3-Hexene	1.89	0.86	0.12
Methoxy Cyclohexane	1.43	1.68	0.11
Toluene	0.22	-	0.14
Pentane	0.38	0.18	-
Methyl Cyclopentane	0.18	0.08	0.01
Methane	7.93	5.64	4.93

Table S11. Catalytic performance data from the *m*-cresol HDO reaction at 350 °C, 0.5 MPa, 8:1 H_2:*m*-cresol molar ratio, WHSV = 5 h^{-1}, presented as an average between 290 and 460 min time-on-stream for the series of SiO_2-supported Ni_2P, $Ni_{2-x}Rh_xP$, and Rh_2P catalysts.

	Ni_2P	**$Ni_{1.8}Rh_{0.2}P$**	**$Ni_{1.6}Rh_{0.4}P$**	**$Ni_{1.4}Rh_{0.6}P$**	**$Ni_{1.2}Rh_{0.8}P$**	**Rh_2P**
Conversion (%)	7.71	11.29	7.78	9.91	13.91	9.32
STY (s^{-1})	6.8 x 10^{-2}	8.3 x 10^{-2}	6.4 x 10^{-2}	9.6 x 10^{-2}	9.7 x 10^{-2}	3.8 x 10^{-2}
Total Carbon Product Selectivity (%)						
Cyclohexane	1.35	0.87	0.47	1.00	0.82	0.37
Methylcyclohexane	3.51	2.81	1.75	1.68	1.63	0.66
Methylcyclohexene	8.77	7.99	17.9	10.6	6.38	2.95
Benzene	0.63	0.83	0.32	0.62	0.65	0.26
Toluene	35.2	33.7	29.1	21.2	29.7	78.0
Xylene (isomers)	0.89	0.85	0.56	1.30	1.55	0.41
Cyclohexanol	0.01	0.01	0.00	0.01	0.00	0.00
Methylcyclohexanol	0.86	4.27	2.31	6.58	7.56	0.10
Cyclohexanone	0.02	0.02	0.01	0.03	0.01	0.01
Methylcyclohexanone	30.4	33.9	37.8	40.4	37.4	5.14
Light hydrocarbons (C1-C5)	10.5	13.6	4.99	13.7	12.2	10.8

Table S12. Hydrogenation (HYD) and direct deoxygenation (DDO) pathway selectivities calculated using the product selectivities tabulated in Table S10. Pathway selectivity to HYD included methylcyclohexanone, methylcyclohexanol, methylcyclohexene, and methylcyclohexane. Pathway selectivity to DDO included toluene, benzene, and xylene.

	Ni_2P	**$Ni_{1.8}Rh_{0.2}P$**	**$Ni_{1.6}Rh_{0.4}P/SiO_2$**	**$Ni_{1.4}Rh_{0.6}P/SiO_2$**	**$Ni_{1.2}Rh_{0.8}P/SiO_2$**	**Rh_2P/SiO_2**
HYD	54.3	58.0	66.6	71.9	62.4	10.1
DDO	45.7	42.0	33.4	28.1	37.6	89.9

Table S13. DFT-calculated lattice parameters (*a* and *c*, in Å) for bulk $Ni_{2-x}Rh_xP$ (x = 0, 0.17, 0.33, 0.50, 0.67, 0.83, 2). Experimental lattice parameters are provided for the parent Ni_2P and Rh_2P bulk materials.

	a (*c*), Å	
x	**DFT**	**Experimental**
0	5.80 (3.35)	5.86 (3.38)[23]
0.17	5.83 (3.37)	
0.33	5.86 (3.38)	
0.50	5.88 (3.40)	
0.67	5.90 (3.41)	
0.83	5.93 (3.42)	
2	5.50	5.50[24]

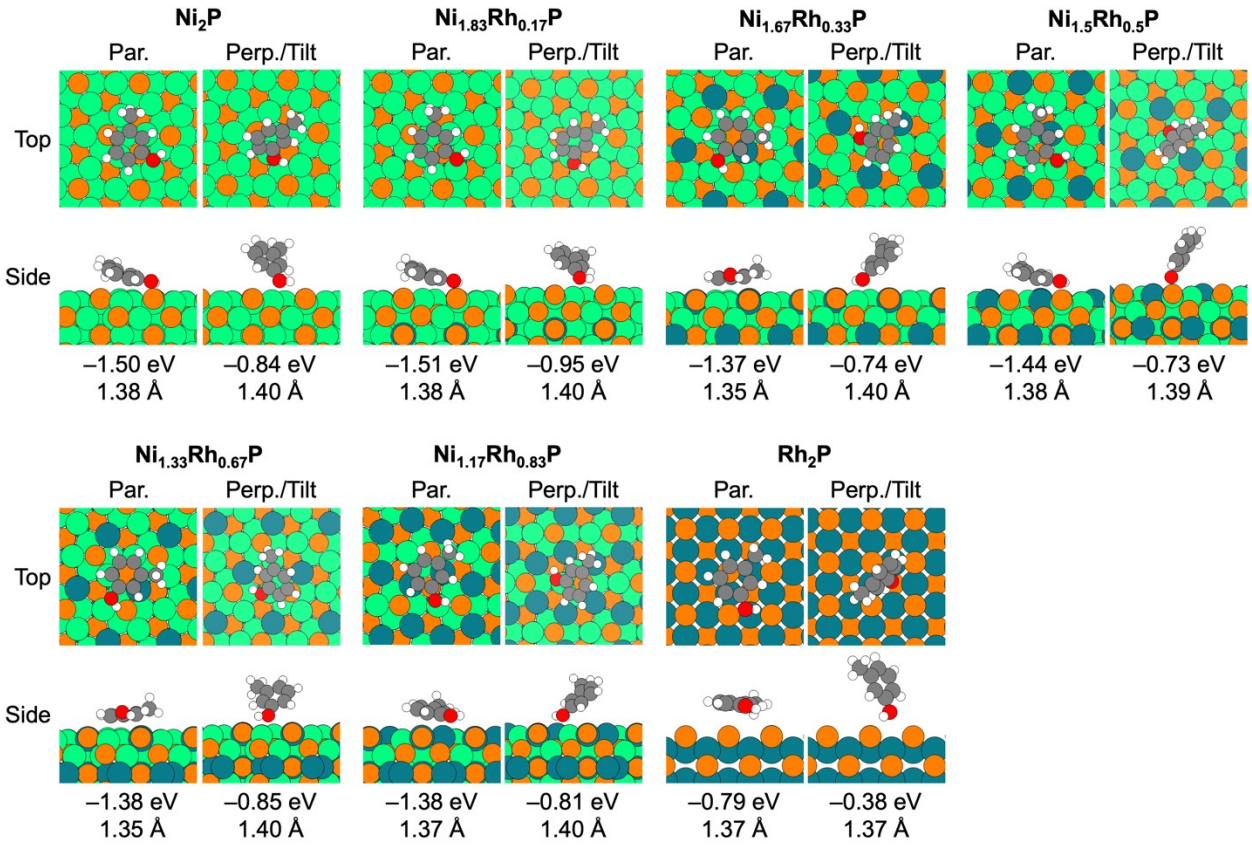

Figure S18. Top and side views of *m*-cresol* adsorption on Ni_3P-terminated $Ni_{2-x}Rh_xP(0001)$ (x = 0, 0.17, 0.33, 0.5, 0.67, 0.83) and P-terminated $Rh_2P(100)$ (x = 2.0) in both parallel (Par.) and perpendicular/tilted (Perp./Tilt) adsorption configurations. Adsorption energies and Ph–OH bond distances are provided below each configuration. Atom colors: orange – P, green – Ni, teal – Rh, grey – C, white – H, red – O

Table S14. Adsorption energies (E_B, in eV) for OH* on Ni_3P-terminated $Ni_2P(0001)$ with the lattice constant of the corresponding $Ni_{2-x}Rh_xP(0001)$ surface (x = 0.17, 0.33, 0.50, 0.67, 0.83).

x	E_B(OH) (eV)
0.17	–3.43
0.33	–3.42
0.50	–3.40
0.67	–3.39
0.83	–3.38

References

1. Cai, Z.; Chattopadhyay, N.; Liu, W.J.; Chan, C.; Pignol, J-P.; Reilly, R.M. Optimized digital counting colonies of clonogenic assays using ImageJ software and customized macros: Comparison with manual counting. *Int. J. Radiat. Biol.* **2011**, *87*, 1135–1146.

2. Lutterotti, L.; Bortolotti, M. Object-oriented programming and fast computation techniques in Maud, a program for powder diffraction analysis written in Java. *Int. Union Crystallogr.* **2003**.

3. Chupas, P.J.; Chapman, K.W.; Jennings, G.; Lee, P.L.; Grey, C.P. Watching nanoparticles grow: The mechanism and kinetics for the formation of TiO_2-supported platinum nanoparticles. *J. Am. Chem. Soc.* **2007**, *129*, 13822–13824.

4. Juhás, P.; Davis, T.; Farrow, C.L.; Billinge, S.J.L. PDFgetX3: A rapid and highly automatable program for processing powder diffraction data into total scattering pair distribution functions. *J. Appl. Crystallogr.* **2013**, *46*, 560–566.
5. Aoun, B. Fullrmc, A rigid body reverse monte carlo modeling package enabled with machine learning and artificial intelligence. *J. Comput. Chem.***2016**, *37*, 1102–1111.

6. Neugebauer, J.; Scheffler, M. Adsorbate-substrate and adsorbate-adsorbate interactions of Na and K adlayers on Al(111). *Phys. Rev. B.* **1992**, *46*, 16067–16080.

7. Bengtsson, L. Dipole correction for surface supercell calculations. *Phys. Rev. B.* **1999**, *59*, 12301–12304.

8. Tang, W.; Sanville, E.; Henkelman, G. A grid-based Bader analysis algorithm without lattice bias. *J. Phys. Condens. Matter.* **2009**, *21*, 084204.

9. Sanville, E.; Kenny, S.D.; Smith, R.; Henkelman, G. Improved grid-based algorithm for Bader charge allocation. *J. Computational Chem C.* **2007**.

10. Henkelman, G.; Arnaldsson, A.; Jónsson, H. A fast and robust algorithm for Bader decomposition of charge density. *Comput. Mater. Sci.* **2006**, *36*, 354–360.

11. Yu, M.; Trinkle, D.R. Accurate and efficient algorithm for Bader charge integration. *J. Chem. Phys.* **2011**, *134*, 064111.

12. Nørskov, J. K.; Abild-Pedersen, F.; Studt, F.; Bligaard, T. Density functional theory in surface chemistry and catalysis. *Proc. Natl. Acad. Sci.* **2011**, *108*, 937–943.

13. Michalsky, R.; Zhang, Y.-J.; Medford, A.J.; Peterson, A.A. Departures from the adsorption energy scaling relations for metal carbide catalysts. *J. Phys. Chem. C*. **2014**, *118*, 13026–13034.

14. Wang, X.; Wan, F.; Gao, Y.; Liu, J.; Jiang, K. Synthesis of high-quality Ni_2P hollow sphere via a template-free surfactant-assisted solvothermal route. *J. Cryst. Growth.* **2008**, *310*, 2569–2574.

15. Secoue, M.; Auvray, P.; Toudic, Y.; Ballini, Y.; Guerin, R. Synthesis, lattice parameters and thermal expansion coefficients of rhodium arsenide Rh_2As and some substituted compounds. *J. Cryst. Growth*. **1986**, *76*, 135–141.